

Determining local mobility variation along recrystallization boundaries

Jin Zhang^a, Yubin Zhang^{b,*}

^aDepartment of Materials Science and Engineering, Northwestern University, Evanston, 60208, IL, USA

^bDepartment of Civil and Mechanical Engineering, Technical University of Denmark, Kgs. Lyngby, 2800, Denmark

Abstract

Understanding recrystallization boundary migration mechanisms is crucial for materials design. However, the lack of comprehensive mobility data for high-angle grain boundaries in typical polycrystalline samples has impeded gaining insights into the factors that govern boundary migration. In this work, we develop a fitting methodology to determine mobility values for individual recrystallization boundaries in partially recrystallized samples. This methodology involves optimizing mobility inputs in a phase field model by aligning simulated microstructure with time-series recrystallization experiments. We first validate this method on synthetic data and then apply it to real experimental data. For the first time, we reveal a three-order-magnitude variation in local mobility along individual recrystallization boundaries. Additionally, we provide detailed analytical and computational analyses to explore the effect of this local mobility variation on boundary migration. The results show that mobility variation significantly influences boundary dynamics, shedding light on the interplay of factors that impact the observed boundary migration behavior. This methodology offers a new framework for interpreting experimental recrystallization behavior and can be broadly applied to other materials using *in situ* experiments.

Keywords: Recrystallization, Phase field, Grain boundary, Grain boundary mobility, Analytical method

1. Introduction

Recrystallization is vital for optimizing material microstructure and enhancing properties [1]. This process involves the formation and growth of nearly defect-free nuclei, facilitated by the migration of recrystallization boundaries. It is crucial to understand how these boundaries migrate to control the microstructure and tailor the resulting material's performance. The local migration velocity of these boundaries, v , is governed by the equation:

$$v = MF = M(F_s + F_\sigma), \quad (1)$$

where M is the mobility, and F is the driving force for migration [2]. The driving force consists of the stored energy in the deformed matrix F_s and the boundary-curvature-based driving force $F_\sigma = \sigma\kappa$. Here, σ is the grain boundary energy, and κ is the total curvature, defined to be negative for a sphere. The curvature driving force was overlooked in the literature but has been emphasized to be significant for accurately quantifying local boundary migration [3, 4, 5, 6].

It is critical to understand the different contributions to the boundary migration velocity to comprehend their role in the recrystallization microstructure. The local stored energy in the deformed matrix F_s can be quantified by electron microscopes, and the boundary curvature κ at discrete time steps can be determined from the experimental microstructure. However, despite its importance, there is limited research on the

recrystallization boundary mobility. The mobility M depends on the crystallography of the boundary and various physical factors. A comprehensive understanding of M requires determining a large amount of mobility data. Current research primarily focuses on bi-crystals [7, 8, 9, 10] and molecular dynamics [11, 12, 13, 14], which have mainly explored a limited number of boundaries with special misorientations and geometries, providing inadequate insight into the migration behavior of recrystallization boundaries with arbitrary misorientations and geometries in real polycrystalline materials. Existing mobility measurements typically rely on averaging across multiple grains using the average driving force over the entire sample, thus concealing the variability in mobility among different boundaries [15, 16, 17, 18]. Recently, average mobilities have been quantified for individual recrystallization boundaries through *ex situ* experiments that measure local boundary migration [19, 20, 21]. However, as a recrystallizing grain grows into the deformed matrix, misorientation varies for individual dislocation cells along the boundary. It is currently unknown whether this misorientation variation corresponds to a mobility variation and how it affects local boundary migration.

The aim of this work is to develop a method for quantifying the local mobility variation along individual recrystallization boundaries. The method uses experimental data as input for a phase field simulation. This simulation is used to fit mobility values for each boundary segment of the recrystallizing grain encountered during the migration process, ensuring that the simulated migration aligns with the experimental boundary migration process. This fitting approach is illustrated in Fig. 1. The mobility input for the simulation is refined during the optimization to minimize a cost function, with those

*Corresponding author

Email addresses: jzhang@northwestern.edu (Jin Zhang), yubz@dtu.dk (Yubin Zhang)

at the minimum being regarded as the physical mobility value. The experimentally measured stored energy F_s is used directly in the simulation, and the local velocity and curvature values between any two experimental steps are interpolated using the phase field model. This allows for the separation of different contributions to the migration velocity in Eq. 1.

This method is inspired by our previous works on determining materials parameters from *in situ* experiments for the liquid diffusion coefficient [22] and reduced grain boundary mobility during grain growth [23]. However, the present study utilizes unique properties of recrystallization that are not present in previous studies. For example, a stored-energy driving force must be considered in addition to the curvature driving force. Additionally, an extension method [24] is used to project the interfacial mobilities to the whole computational domain, preventing the need to consider each grain or subgrain as separate order parameters. Furthermore, an efficient optimization algorithm is proposed without solving the computationally expensive sensitivity equations.

To validate the proposed fitting method, we first use synthetic data with known ground-truth mobility values. Subsequently, we use time-series experimental data that investigated the migration process of a general high-angle recrystallization boundary during *ex situ* annealing of pure aluminum [19]. The mobility values of each pixel swept by the recrystallization boundary are then determined using the proposed method. The result shows that local mobility can vary by more than three orders of magnitude along a single recrystallization boundary. The mobility generally correlates well with misorientation, but the pattern is rather complex, indicating the effect of other factors.

2. Methodology

This section presents the fitting method, which consists of three main components: experimental data (boundary migration, stored energy and misorientation), a phase field model, and an optimization method. These components are illustrated in Fig. 1. While the boundary migration data will be detailed in subsequent sections, the latter two components are covered here, with a focus on the fundamental elements of the optimization method. These elements include the design variable, the objective function, the sensitivity analysis, and the optimization algorithm.

2.1. Phase field model for recrystallization

This work uses a driven Allen-Cahn equation to simulate the recrystallization process. The boundary migration is modeled using the following phase field equation

$$\frac{\partial u}{\partial t} = \mathcal{P}_u(M) \left(\frac{p'(u)}{6\ell} F_s + \sigma \left(\vec{\nabla}^2 u - \frac{1}{2\ell^2} g'(u) \right) \right), \quad (2)$$

where $M(\vec{x})$ is the mobility, $u(\vec{x}, t)$ is the phase field variable, which equals one in the deformed phase and zero in the recrystallized phase, with a smooth transition at the interface over a length scale ℓ referred to as the diffuse interface width, $g(u) = u^2(1-u)^2$ is a double-well potential, $p(u) = u^2(3-2u)$ is an interpolation function. $F_s(\vec{x})$ has the same meaning as in

Eq. 1. Here, the mobility $M(\vec{x})$ is defined as the mobility if the recrystallization boundary is located at \vec{x} . Therefore, in Eq. 2, we should only use the mobility where the boundary is currently located. To account for this, we introduce a projection operator $\mathcal{P}_{u(\vec{x}, t)}(\cdot)$ to map the mobility at the current boundary (given by $u(\vec{x}, t) = 0.5$) to every point in the computational domain by making $\mathcal{P}_u(M)$ a constant perpendicular to the boundary. An example is given in Supplementary Fig. S1. Note this projection is needed for each time step. More details on the projection operator can be found in [24]. Equation 2 can be seen as a diffuse interface version of the sharp interface model in Eq. 1. The derivative of the interpolation $p'(u)$ in Eq. 2 can be viewed as a regularized Dirac-delta function to localize the driving force close to the interface. The term in the bracket after σ can be viewed as the diffuse interface version of the total curvature. By using Eq. 2 instead of Eq. 1, we prevent the need to track the interface explicitly. Moreover, it is unnecessary to calculate ν and κ explicitly as they are embedded into the phase field equation.

2.2. Optimization problem

The goal of the fitting is to find a set of mobilities, denoted as $\mathbf{M} = \{M_\delta | \delta = 1, \dots, n\}$, that minimizes the difference between the simulated boundary migration path $u(t_k; \mathbf{M})$ and the experimentally measured time series of boundary traces. These optimal mobilities are regarded as the physical materials parameters. The experimental microstructure is described by the signed distance functions $\phi_{\text{exp}}(t_k)$, where t_k is the k -th experimental time step. The optimization problem is defined as

$$\begin{aligned} & \text{find } \mathbf{M} = \{M_1, M_2, \dots, M_n\} \\ & \text{minimize } f_{\text{cost}}(u(t_k; \mathbf{M}), \phi_{\text{exp}}(t_k)) \\ & \text{such that } G(u(t_k; \mathbf{M}), \mathbf{M}) = 0, \end{aligned} \quad (3)$$

where f_{cost} is the objective function that measures the difference between the simulation and the experiment, which will be discussed later. The constraint function is

$$G(u(t_k; \mathbf{M}), \mathbf{M}) = u(t_k) - u(\phi_{\text{exp}}(t_0)) - \int_{t_0}^{t_k} \frac{\partial u}{\partial t} dt, \quad (4)$$

which enforces that u satisfies the phase field equation (Eq. 2).

2.3. Design variables

After discretization of Eq. 2, a mobility $M_i = M(\vec{x}_i)$ is assigned to each cell, where a cell corresponds to the computational grid. Here, \vec{x}_i is the location of the i -th cell. In this work, the computational grid size matches the experimental resolution, so the cell also represents a pixel/voxel in the 2D/3D experimental image. Though M_i seems to be a natural choice of the design variable, it results in a huge design space that can easily lead to overfitting. Therefore, instead, we define the design variable M_δ at given sampling points in the misorientation space, as shown in Fig. 1. This approach helps to regularize the problem by using mobilities of fewer sampling points (red points in Fig. 1).

To interchange the mobilities defined at sampling points M_δ

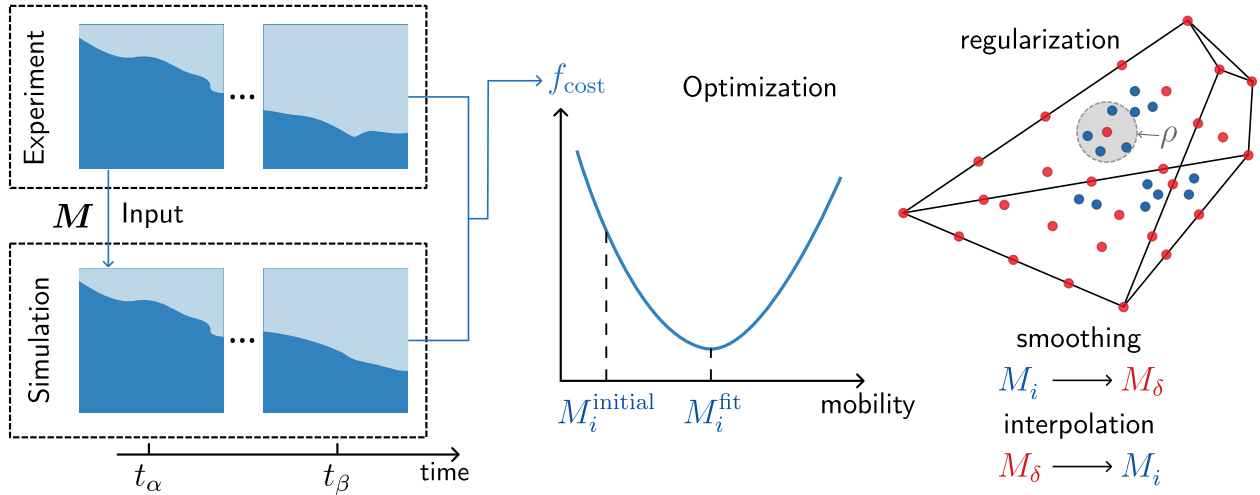


Fig. 1. Fitting method. The evolution of the recrystallized boundary is measured experimentally. Taking one experimental snapshot (t_α) as input, the evolution of the recrystallized boundary is simulated with a guess of the mobility parameters \mathbf{M} and compared with the experiment at t_β to define a cost function f_{cost} , quantifying their dissimilarity. An optimization algorithm minimizes the cost function and determines the mobility M_i^{fit} that best matches the simulation with the experiment. The fitted mobilities M_i are regularized in the Rodrigues-Frank space using sampling points (red points). Data points (blue points; related to each pixel) within a regularization radius ρ to a sampling point in the misorientation space are used for regularization. The regularized mobilities M_δ are then interpolated to update the mobility guess at each pixel M_i . The whole process is repeated until convergence.

with those at each cell M_i (referred to as data points), we introduce the following smoothing and interpolation processes

$$M_\delta = \frac{\sum_{|\vec{R}_i - \vec{R}_\delta| < \rho} w_i M_i}{\sum_{|\vec{R}_i - \vec{R}_\delta| < \rho} w_i}, \quad (5a)$$

$$M_i = \sum_{\delta=1}^n w_\delta(\vec{R}_i) M_\delta, \quad (5b)$$

where \vec{R}_δ is the misorientation of a sampling point, $\vec{R}_i = \vec{R}(\vec{x}_i)$ is the misorientation of a data point determined experimentally, w_δ is the interpolation weighting factor, w_i is the smoothing weighting factor, and ρ is the radius of a sphere centered at the sampling point \vec{R}_δ in the misorientation space. The smoothing process includes all neighboring data points within the sphere of radius ρ , as shown in Fig. 1. In this work, linear interpolation is used in Eq. 5b, and w_i is determined from the distance from this data point \vec{R}_i to the sampling point \vec{R}_δ : $w_i = \text{dist}(\vec{R}_\delta, \vec{R}_i)$.

2.4. Objective function

The objective function quantifies the dissimilarity between the simulated microstructure represented by u and the experimentally measured microstructure ϕ_{exp} at three levels:

$$f_{\text{cost}}^{\text{local},\alpha\beta}(\vec{x}) = |\phi_{\text{sim}}(u(\vec{x}, t_\beta; \mathbf{M})) - \phi_{\text{exp}}(\vec{x}, t_\beta)|^2, \quad (6a)$$

$$f_{\text{cost}}^{\alpha\beta} = \int_{\Omega_{\alpha\beta}} f_{\text{cost}}^{\text{local},\alpha\beta}(\vec{x}) dV, \quad (6b)$$

$$f_{\text{cost}} = \sum_{\alpha < \beta} f_{\text{cost}}^{\alpha\beta}, \quad (6c)$$

where the local cost function $f_{\text{cost}}^{\text{local},\alpha\beta}$ is defined for each cell, the cost function $f_{\text{cost}}^{\alpha\beta}$ encompasses all cells for a given combination of experimental time steps $t_\alpha < t_\beta$, and the total cost function f_{cost} comprises a given set of combinations of experimental time

steps. The simulation starts from an initial condition given by $\phi_{\text{exp}}(t_\alpha)$, and the comparison with the experiment is performed at time t_β . $\Omega_{\alpha\beta}$ is the domain swept by the measured boundary between t_α and t_β , and the signed-distance function ϕ is related to the phase field u by the hyperbolic tangent profile: $u(\phi) = \frac{1}{2} \left(1 - \tanh \frac{\phi}{2\ell} \right)$.

2.5. Sensitivity analysis

Sensitivity is the gradient of a function in the design space. Sensitivity analysis is a key step in constructing an optimization algorithm because it provides information on how a function responds to small changes in each design variable. The sensitivity of the cost function derived using the adjoint method [25] is

$$\frac{d f_{\text{cost}}^{\alpha\beta}}{d\mathbf{M}} = - \frac{d f_{\text{cost}}^{\alpha\beta}}{du(\vec{x}, t_\beta)} \frac{\partial G(\vec{x})}{\partial \mathbf{M}} \Big|_{t=t_\beta}, \quad (7)$$

where the sensitivity of the constraint function $\partial G / \partial \mathbf{M}$ is determined from the following evolution equation

$$\frac{\partial}{\partial t} \left(\frac{\partial G}{\partial \mathbf{M}} \right) = - \frac{\partial \mathbf{M}}{\partial \mathbf{M}} \left(\frac{p'(u)}{6\ell} F_s + \sigma \left(\nabla^2 u - \frac{1}{2\ell^2} g'(u) \right) \right), \quad (8a)$$

$$\frac{\partial G}{\partial \mathbf{M}} \Big|_{t=t_\alpha} = 0. \quad (8b)$$

The sensitivity equation (Eq. 8) includes n equations, where n is the number of sampling points, typically around 1000. Solving all the sensitivity evolution equations is computationally expensive, if not prohibited. However, $\partial \mathbf{M} / \partial \mathbf{M}$ is extremely sparse and localized: $\partial \mathbf{M}(\vec{x}) / \partial M_i = \delta(\vec{x} - \vec{x}_i)$, leading to the assumption that M_i only affects the local cost function at \vec{x}_i . This assumption leads to a scaling property, which applies to each cell:

$$f_{\text{cost}}^{\text{local},\alpha\beta}(t, kM_i) = f_{\text{cost}}^{\text{local},\alpha\beta}(kt, M_i), \quad (9)$$

where k is an arbitrary positive constant. This property is similar to the one used in our previous works [22, 23].

2.6. Optimization algorithm

The optimization algorithm is constructed around the scaling property (Eq. 9), which transfers the derivative with respect to the design variable (sensitivity) to a time derivative. As the scaling property is an approximation, an iterative optimization process is necessary to find the optimal mobilities. Using this idea, the optimization problem can be solved by only solving the phase field equation, without resolving the time-consuming sensitivity evolution in Eq. 8. The optimization algorithm consists of the following steps

1. Initialize the optimization with an initial guess of the mobilities $M_\delta = M_i = M^{\text{initial}}$.
2. Solve the phase field equation (Eq. 2) with the mobilities M_i .
3. Fit the mobility of each cell M_i based on the scaling property (Eq. 9). The readers can refer to [22, 26, 23] for more details on the local fitting process.
4. Determine the mobilities at sampling points in the fundamental zone of the Rodrigues space M_δ from the mobilities of all neighboring cells M_i by the smoothing given in Eq. 5a.
5. Update the mobility of each cell M_i by interpolating the sampling points using Eq. 5b.
6. Go to step 2 and repeat this process until convergence.

3. Validation of the fitting method using synthetic data

The proposed fitting method is first validated using synthetic data generated by the phase field model, where ground truth mobility values are known.

The synthetic stored energy is shown in Fig. 2a. We assume the mobility has the form [27]

$$M = M_0 \left(1 - \exp \left[-B \left(\frac{\theta}{\theta_m} \right)^n \right] \right), \quad (10)$$

where $B = 5$, $n = 4$, $\theta_m = 15^\circ$, and M_0 is the mobility of high-angle boundaries. For simplicity, the mobility only depends on the misorientation angle, and we select an arbitrary orientation axis $\langle 111 \rangle$ to complete the definition of \vec{R} . The ground-truth mobility is depicted in Fig. 2b. Starting with the initial boundary (dashed line in Fig. 2b), we solve the phase field equation in Eq. 2 to generate the boundary trace with fixed time intervals (solid lines). To simplify the process for this test, the mobility and driving force are nondimensionalized by M_0 and $6\sigma/\ell$, respectively, equivalent to a constant scaling in time. The system consists of 100×200 grids with a grid size of $1 \mu\text{m}$. We employ forward-Euler time integration with adaptive time step cutback to restrict the maximum change of the phase field variable in each time step to 0.01. A linear extension boundary condition in Appendix C is used.

For fitting, the phase field simulation is conducted with an initial microstructure at t_α , and the fitting is performed at $t_{\alpha+1}$, where $\alpha = 0, 1, 2$. For each combination $(t_\alpha, t_{\alpha+1})$, the mobility values for cells within the domain swept by the boundary from t_α to $t_{\alpha+1}$ are fitted and used for the regularization in Eq. 5a. We use a misorientation interval of 1 degree in the Rodrigues-Frank

space to generate sampling points and a regularization radius $\rho = 0.00467$ (approximately 0.5 degrees). With the initial guess of mobilities $M_\delta = 0.5$, Fig. 2c compares the simulated microstructures (dashed lines) and the synthetic ‘experiment’ data (solid lines) at t_1 to t_3 . After five optimization iterations, the fitting method improves the match between simulation and ‘experiment,’ as shown in Fig. 2d. The convergence history of the fitted boundary traces is provided in Supplementary Video S1. Fast convergence is observed for four examples in Fig. 2e (the dashed lines showing the ground truth), indicating the efficiency of the proposed optimization algorithm. Most mobilities are already close to their ground truth with just one iteration. Moreover, the fitting is not sensitive to the initial guess, as shown in Supplementary Fig. S2. The fitted mobilities as a function of the misorientation angle are shown in Fig. 2f and compared with the ground truth given by Eq. 10. A good match with the ground truth is observed, and the low- and high-mobility regions are correctly identified by the fitting method. This test validates the efficiency of the proposed fitting method in determining boundary mobilities.

4. Extracting mobility values based on time-series experimental data

We now apply the fitting method to the experimental data. To test the robustness of the proposed method, we will investigate the effect of various parameters, specifically the effect of filter size in processing the stored energy and the element size in discretizing the Rodrigues space.

4.1. Recrystallization experiment

We use time-series experimental data following the migration of a recrystallization boundary during *ex situ* annealing. A brief overview of the experiment is outlined below, with further details available in [19]. The experiment involved high-purity (99.996%) aluminum with an initial grain size of several millimeters. The sample underwent a 50% cold rolling deformation, followed by a recrystallization heat treatment at 250°C for 10 min in an air furnace. To identify a migrating recrystallization boundary, the sample was electropolished and annealed again at 250°C for 15 minutes. The microstructure around the selected boundary was characterized using electron channeling contrast (ECC) and electron backscatter diffraction (EBSD) techniques in a Zeiss Supra scanning electron microscope. However, due to the thermal and mechanical drift of the beam and sample, the EBSD map exhibited spatial distortion compared to the ECC image. This distortion was corrected using the method presented in [28] based on the ECC image of the corresponding area. The migration of the chosen recrystallization boundary was subsequently monitored using ECC in an *ex situ* manner, with measurements performed in six steps following annealing at 250°C for 15 minutes. The initial microstructure and the traces of the migrating recrystallization boundary are shown in Fig. 3a. The misorientation angle and axis are determined from the EBSD map and shown in Figs. 3a and 3b. The stored energy, F_s , input for the phase field simulation, was calculated using the EBSD map. For this calcula-

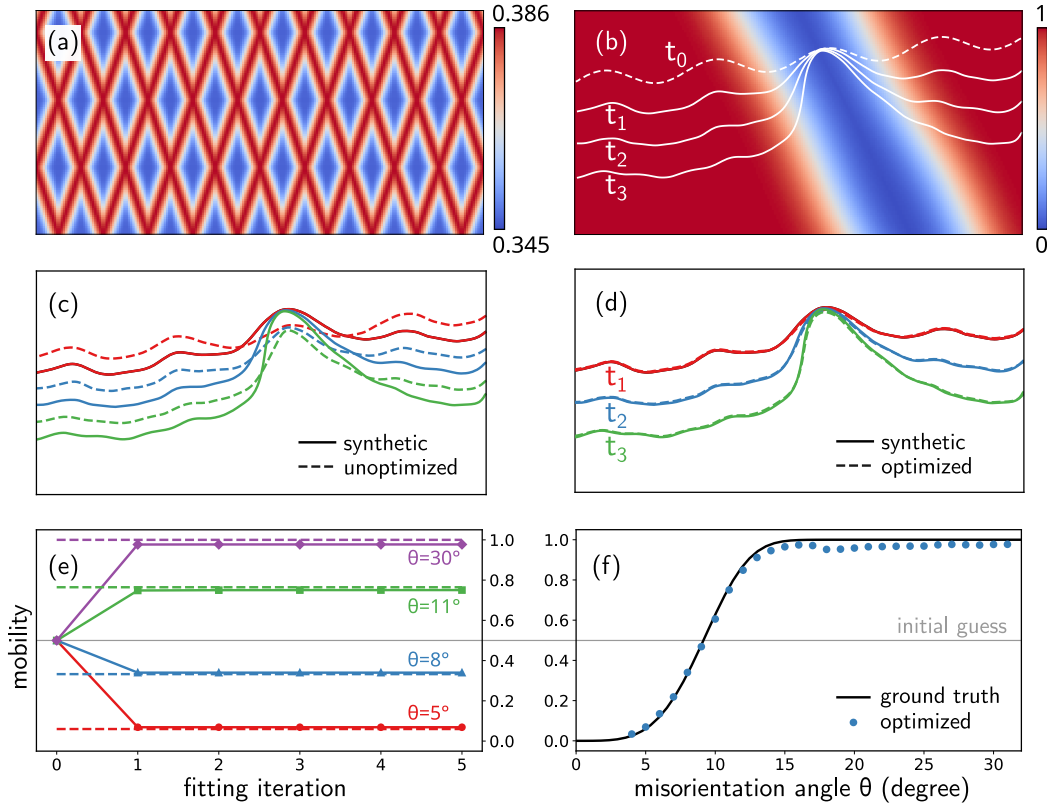


Fig. 2. Fitting with synthetic data. (a) The synthetic stored energy. (b) The ground-truth mobility with overlaid boundary curves. (c) Simulated boundary evolution with the initial guess (unoptimized mobilities) by the dashed lines along with the synthetic data (solid lines). (d) Comparison of the fitted boundary with the experiment. (e) Convergence curves of four sample points with dashed lines representing the corresponding ground truth values. (f) Comparison of the fitted mobility (circular points) with the ground truth (solid line).

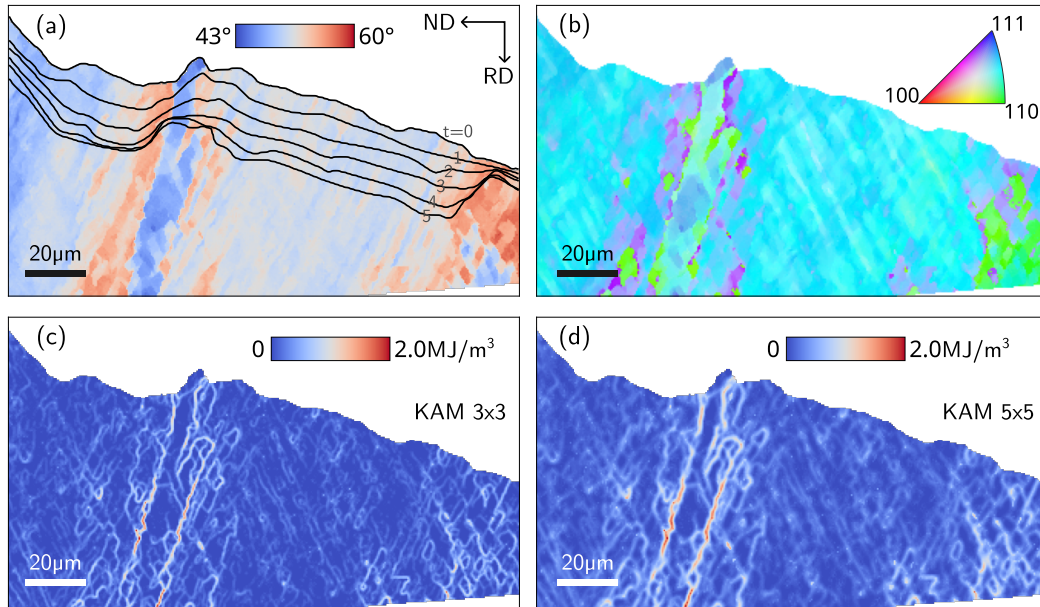


Fig. 3. Recrystallization experiment. (a) Misorientation angle with boundary trace overlaid. (b) Misorientation axis. (c,d) Stored-energy map processed by KAM with (c) 3×3 and (d) 5×5 sized filters. RD: rolling direction, ND: normal direction.

tion, the local stored-energy density for each pixel in the deformed matrix was determined using the method described in [29], based on the kernel average misorientation (KAM) calculated with a subset of either 3×3 or 5×5 centered at the

selected pixel. To reduce orientation noise, the EBSD map was first processed with a Kuwahara filter [30, 31]. All dislocation boundaries with misorientations $\geq 1^\circ$ were considered, with the boundary energy calculated based on the misorientation angle

Table 1. Regularization parameters for two sampling schemes.

Parameter name	Case 1	Case 2
Element size in Rodrigues space e	0.005	0.01
Regularization radius ρ	0.004	0.008
Number of sampling points	2089	599
Average data points per sampling point	11	40

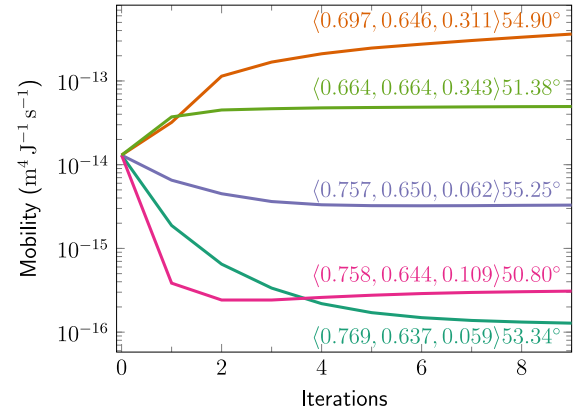
using the Read-Shockley equation, where maximum energy of $\sigma_{\max} = 0.324 \text{ J m}^{-2}$ for boundaries with misorientations higher than 15° was used. The processed stored energy for the 3×3 and 5×5 filters are shown in Figs. 3c and 3d, respectively. We will test the effect of different filter sizes on the fitting results.

4.2. Phase field simulation setup

The simulation domain consists of 190×340 grids with a grid size the same as the experimental resolution, $0.5 \mu\text{m}$. The adaptive time stepping method is the same as in the previous section. Since the recrystallization boundaries are high-angle ($44.1 - 57.6^\circ$) and far from special (Σ) boundaries, we assume constant grain boundary energy $\sigma = 0.324 \text{ J m}^{-2}$ [19]. A linear extension boundary condition (see Appendix C for details) at all four outer boundaries is used to approximate the experiment.

4.3. Regularization in the Rodrigues-Frank space

We consider each pixel swept by the recrystallization as an experimental data point. In total, there are 14580 data points. Using these data points directly as design variables can lead to overfitting. To prevent overfitting, we define the design variable on sampling points in the Rodrigues-Frank misorientation space. These sampling points are obtained by discretizing the Rodrigues space, with two average element sizes, $e = 0.005$ and $e = 0.01$, corresponding to misorientation angles of approximately 0.5° and 1° , respectively. An example of the sampling points for $e = 0.01$ is shown in Supplementary Fig. S3a. Since the experiment data only covers a small portion of the Rodrigues space (blue points in Fig. S3b), we only consider sampling points with nearby data points (red points in Fig. S3b). The number of sampling points is much smaller than the data points, and a regularization radius ρ is chosen to ensure a sufficient number of data points are related to each sampling point, as shown in Table 1. A regularization radius $\rho = 0.008$ corresponds to a misorientation angle of about 0.86° . Note that some data points close to the boundary of the ρ sphere belong to more than one sampling point. To minimize the effect of double-counting, the distance between the sampling point \vec{R}_δ and the data point \vec{R}_i is used to determine the weighting factor $w_i = a \text{dist}(\vec{R}_\delta, \vec{R}_i)$, with a prefactor a reflecting the quality of the minimum found from the local fitting in the optimization algorithm (step 3). If no minimum is found, a is set to 0, meaning this data point is not used in smoothing. If a minimum is found and its value is within 0.01 – 100 of the previous mobility guess, a is set to 1; otherwise, a is set to 0.5. In addition, pixels within two grids from the outer boundary of the simulation domain have $a = 0$ to minimize the effect due to boundary conditions. An example of the prefactor a is shown in Supplementary Fig. S4.

**Fig. 4.** Convergence of the fitted mobility for selected sampling points.

4.4. Fitting iterations

We now apply the proposed fitting method to the experimental data in Fig. 3. The initial guess of the mobilities is $M^{\text{initial}} = 1.3 \times 10^{-14} \text{ m}^4 \text{ J}^{-1} \text{ s}^{-1}$. A set of combinations of experimental time steps $\{(t_\alpha, t_\beta) | \alpha = 1, \dots, 4; \beta = \alpha + 1\}$ is used, where t_α is the starting time of the phase field simulation, and t_β is when the fitting is performed. The adjacent time steps are chosen to minimize the effect of experimental uncertainty. The fitting took about two hours to run nine optimization iterations with an Intel Xeon Gold 6338 CPU (64 cores). The proposed algorithm shows fast convergence. Most mobility values converged after nine fitting iterations, with examples shown in Fig. 4. The optimization history of the fitted migration boundary is given in Supplementary Video S2. The convergence history of the mobilities in the Rodrigues space is shown in Supplementary Video S3.

We also study the effect of filter size (used in processing F_s) and element size e (discretization of the Rodrigues space). Two filter sizes, KAM 3×3 and KAM 5×5 , and two element sizes, $e = 0.005$ and $e = 0.01$, are used, resulting in four cases. We compare the optimized boundary migration patterns with the experimentally measured ones in Fig. 5 for the four cases and find a good match for most boundary segments. The match between the simulation and the experiment is characterized by the following evaluation function

$$f_{\text{eval}} = \frac{\sum_{\beta} \int_{|\phi_{\text{exp}}(t_\beta)| < \varepsilon} |\phi_{\text{sim}}(t_\beta; \mathbf{M}_{\text{fit}}) - \phi_{\text{exp}}(t_\beta)| dV}{\sum_{\beta} \int_{|\phi_{\text{exp}}(t_\beta)| < \varepsilon} dV}, \quad (11)$$

where the summation over β accounts for all the experimental time steps used for the fitting, and $\varepsilon = 3\Delta x$ specifies the integral domain as a narrow region around the experimental boundary. The quantity f_{eval} has a physical meaning of the average distance between the simulated and measured boundaries and is shown in Fig. 5 for all cases. The f_{eval} values for each t_β are listed in Supplementary Table S1. Generally, a small filter and element sizes provide a better fitting. We notice some relatively large discrepancies for the boundary segments in the middle-left region even for the best case (gray box in Fig. 5), with the

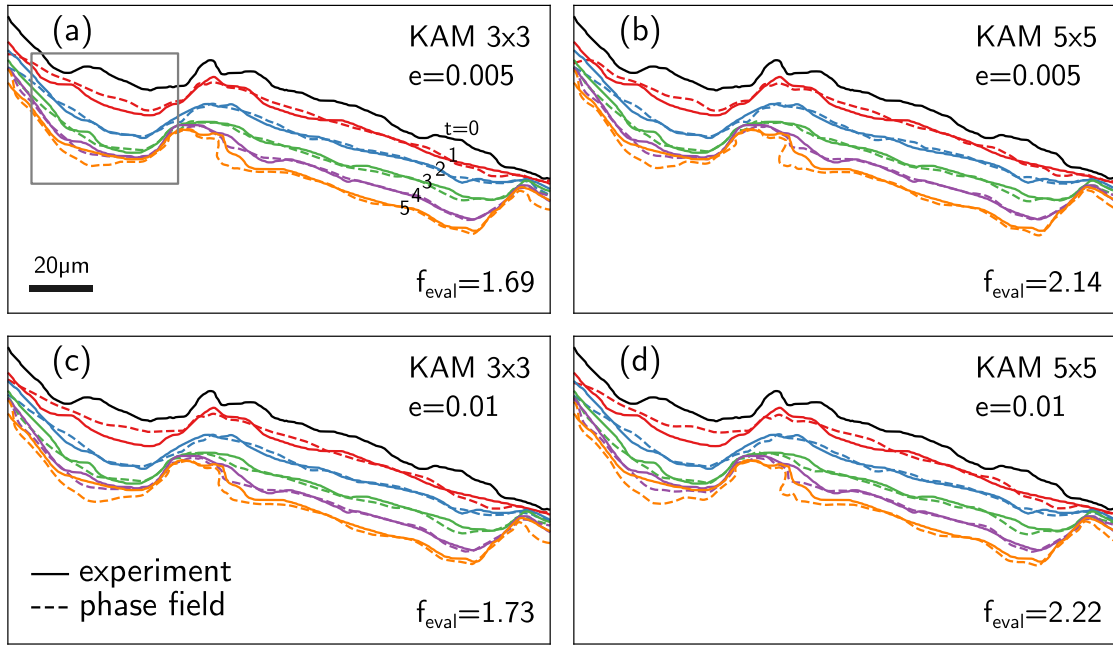


Fig. 5. Comparison of fitted migration boundaries (dashed lines) with experimental measurements (solid lines). Each column corresponds to the stored energy processed by KAM with filters of 3×3 and 5×5 . The first row employs a discretization of the Rodrigues space with an average element size of $e = 0.005$, and the second row uses an average element size of $e = 0.01$. The evaluation function f_{eval} quantifies the quality of the fitting (lower is better).

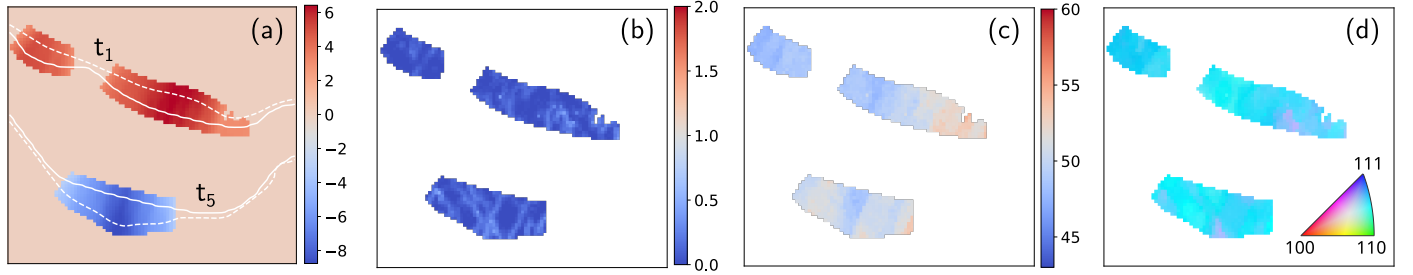


Fig. 6. A closer view of the gray box region in Fig. 5a. (a) The distance between the simulated and experimental boundaries in units of the grid size. Only regions with a difference larger than five grids are shown. At t_1 , the simulation (dashed line) under-predicts the experiment (solid line), while at t_5 , the opposite is observed. (b) The stored energy in the corresponding region with unit MJ m^{-3} . (c) The misorientation angle in degree. (d) The misorientation rotation axis.

largest mismatch at time steps 1 and 5, where the simulation under-predicts the experiment for t_1 and over-predicts for t_5 . A zoom-in view of the region is shown in Fig. 6.

Figure 6a shows the distance between the simulated and experimental microstructures $\phi_{\text{exp}} - \phi_{\text{sim}}(u)$, with a distance larger than three grids displayed. The inclinations of the boundary segments are similar between t_1 and t_5 , and there is no significant difference in the stored energy, as given in Fig. 6b. In addition, the misorientations for the boundary segments do not change much while the boundary is migrating along the rolling direction (RD), as shown in Figs. 6c and 6d. This is further confirmed by comparing the misorientation in Rodrigues-Frank space between t_1 and t_5 shown in Supplementary Fig. S5. The fitting method predicts the migration for the three intermediate time steps in the regions with similar store energies and misorientations; therefore, we suspect that under-prediction and over-prediction for the early and later annealing stages, respectively, might due to other physical driving forces and are not an issue of the fitting approach. One possibility is a different driving force due to local stress states at these two times. Overall, the

fitting method shows that mobility is closely connected with misorientation, though the relationship is complex. In conclusion, the present fitting method works well for the experimental data, and the fitted mobility values are trustworthy.

4.5. Mobility results

Figure 7 shows the fitted mobility interpolated to each pixel of the microstructure. Points that are not converged or have high uncertainty (less than 3 data points inside the ρ -sphere) are not shown. Here, convergence is defined as the change in $\log(M_\delta)$ being less than 0.1. The fitted mobility in Rodrigues space is shown for KAM 3×3 and $e = 0.005$ in Fig. 8a (a 3D view is shown in Supplementary Video S4), with the remaining cases provided in Supplementary Fig. S6. The fitting approach determined 1326 and 457 mobilities simultaneously for $e = 0.005$ and $e = 0.01$, respectively, showing a large mobility variation of about three orders of magnitude. The mobility results are not significantly affected by the filter and element sizes. As expected, the mobility variation decreases with increasing averaging effect in the Rodrigues space (larger e) or

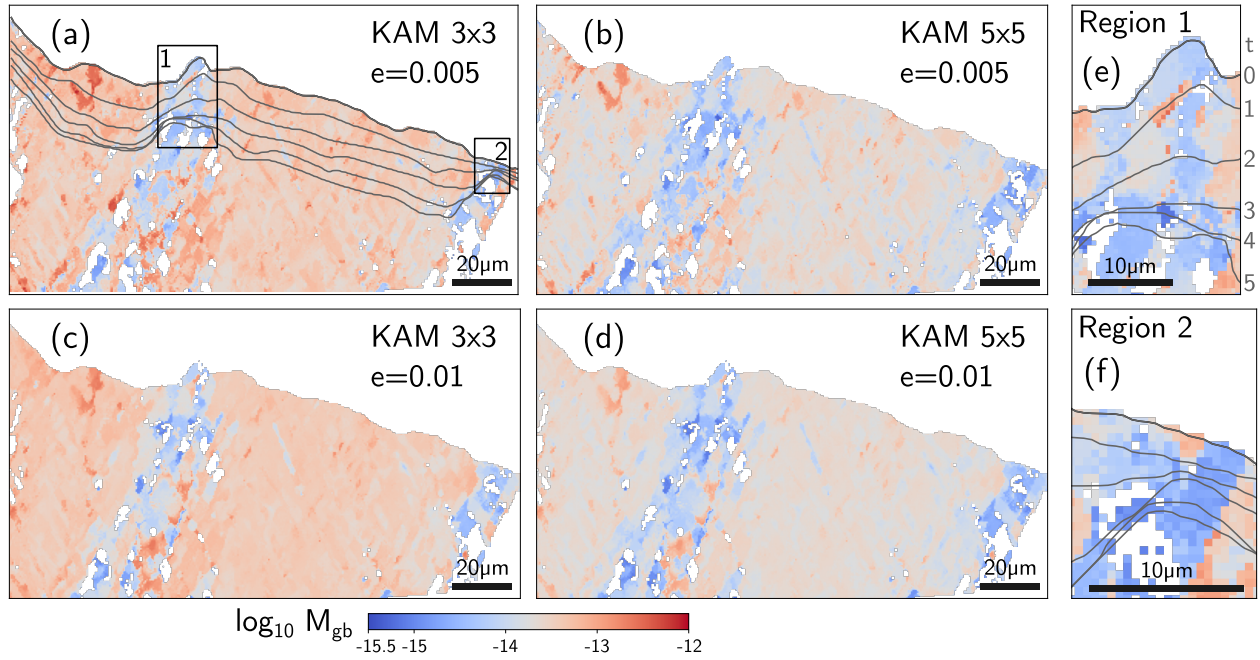


Fig. 7. Comparison of fitted mobilities interpolated to each pixel. Each column corresponds to the stored energy processed by KAM with filters of 3×3 and 5×5 . The first row uses a discretization of the Rodrigues space with an average element size of $e = 0.005$, and the second row uses an average element size of $e = 0.01$. (e,f) Zoom-in view of the two low-mobility regions in (a). The empty pixels are not shown due to a low-quality fitting.

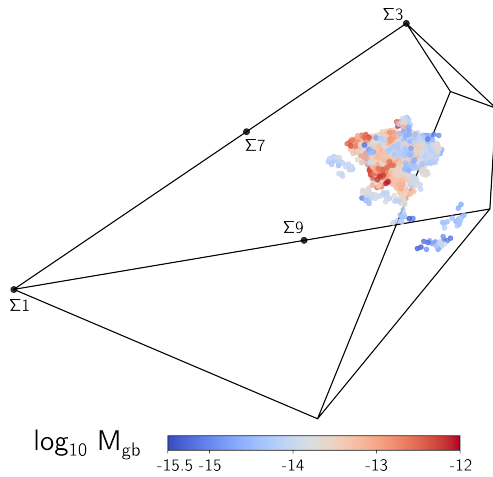


Fig. 8. Fitted mobilities on sampling points in Rodrigues-Frank space for KAM 3×3 filter and an average element size of $e = 0.005$.

the real space (larger filter size). Although the absolute values differ slightly between the four cases, the fitting process identified the same high- and low-mobility regions. It is evident from the band appearance in Fig. 7 that the mobility depends strongly on misorientation. However, the correlation between the two is complex, as revealed in Fig. 8. For better visualization, the highest and lowest mobility points are displayed in Supplementary Fig. S7. The lowest values are mainly close to the $\langle 110 \rangle$ corner, while the highest values are relatively close to the $\langle 111 \rangle$ rotation axis (likely toward $\Sigma 7$ boundaries). The cluster of high-mobility boundaries with a misorientation angle of 52.7° is about 18° from the $\Sigma 7$ boundaries, a well-accepted high-mobility boundary [16].

4.6. Discussion

For the first time, we extract local mobility values for individual recrystallization boundaries based on time-series experimental data. We observe a large local mobility variation, spanning about three orders of magnitude. This range is much larger than, but covers well the range of, the averaged mobility values measured over subset areas of the deformed matrix in [19]: $6.0 \times 10^{-15} - 6.6 \times 10^{-14} \text{ m}^4 \text{ J}^{-1} \text{ s}^{-1}$. By combining Figs. 3 and 7, we are now able to have a detailed analysis of the boundary migration behavior.

In Fig. 7a, the experimentally measured boundary traces are overlaid with the mobility result. The boxes highlight regions with low mobility, showing stagnation in Region 2 but not in Region 1 (during the first three time steps). A closer inspection at Fig. 7a reveals a fundamental difference between these two regions: Region 2 mainly consists of a thicker band with low mobilities, while Region 1 contains bands with a mix of high and low mobilities (see Figs. 7e and 7f for a detailed view). The different migration behaviors in these two regions suggest that the spatial variations in mobility may affect local boundary migration. To explore this further, we present a computational and theoretical study of idealized local mobility variation patterns and apply this understanding to interpret the experiment results in Fig. 7.

To investigate the effect of spatial variation of mobility on boundary migration, we utilize the phase field model in Eq. 2 with a mobility function $M = M_0 + A \cos kx$ (detailed in Appendix A). We set $M_0 = 10^{-14} \text{ m}^4 \text{ J}^{-1} \text{ s}^{-1}$ and assume a constant $F_s = 10^5 \text{ J m}^{-3}$. The grain boundary energy is the same as in Section 4. Figure 9a provides an example of M/M_0 for $A = 0.9M_0$ and $\lambda = 2\pi/k = 10 \mu\text{m}$. Starting with a flat interface at $t = 0$, the evolution of the boundary is depicted in

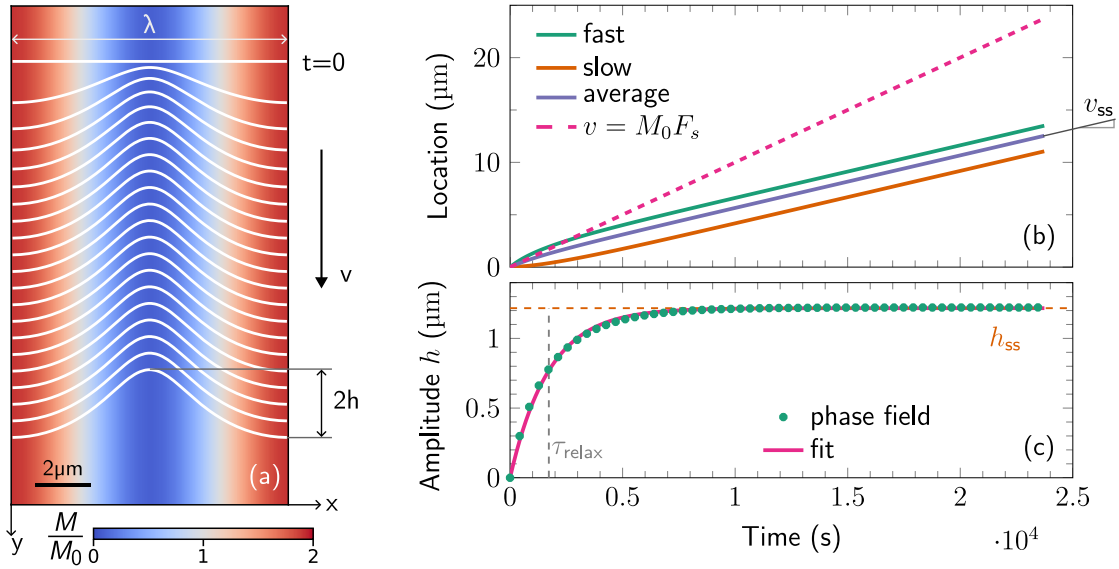


Fig. 9. Phase field study of the effect of spatial mobility variation on boundary migration. (a) History of boundary migration overlaid on the banded mobility pattern with a perturbation amplitude $A = 0.9M_0$ and perturbation wavelength $\lambda = 10 \mu\text{m}$. (b) The change in position of the fast-moving (high mobility), slow-moving (low mobility), and average boundaries over time. The evolution of a boundary without mobility variation ($A = 0$) is indicated by the dashed line. (c) The development of boundary perturbation amplitude. An exponential function is used to fit the phase field points to determine the steady-state amplitude h_{ss} and the relaxation time τ_{relax} .

Fig. 9a. The position of the fast-moving boundary segments (at $x = 0$ and $x = \lambda$), slow segments (at $x = \lambda/2$), and the average interface location are shown in Fig. 9b. It is observed that the fast-moving segments decelerate over time and eventually achieve a steady-state velocity v_{ss} , while the slow-moving segments gradually accelerate and reach the same v_{ss} . In Fig. 9b, the dashed line represents the scenario with no mobility variation ($A = 0$), where the interface moves at a velocity determined by the average mobility M_0 . This result indicates that mobility variation introduces a drag effect, resulting in an overall lower boundary velocity. As seen in Fig. 9a, the boundary shape can be characterized by the wavelength λ and the amplitude h . The time evolution of the amplitude is shown in Fig. 9c, and it is fitted by an exponential function $h(t) = h_{ss}(1 - \exp(-t/\tau_{\text{relax}}))$ to determine the steady-state amplitude h_{ss} and the relaxation time τ_{relax} .

Here, we investigate how mobility variation, including its wavelength λ and amplitude A/M_0 , affect three boundary migration parameters: the steady-state velocity v_{ss} , steady-state amplitude h_{ss} , and the relaxation time τ_{relax} . In Figs. 10a-c, the parameters v_{ss} , h_{ss} , and τ_{relax} are plotted against the mobility perturbation wavelength λ for two amplitudes A . In Figs. 10d-e, the same parameters are displayed as a function of A/M_0 for $\lambda = 2 \mu\text{m}$. In addition, we performed an analytical analysis of the effect of mobility variation, which is detailed in Appendix A. The results are compared with the phase field simulations in Fig. 10. Despite an assumption of small steady-state boundary slope in deriving our analytical expressions, the analytical results show good agreement with the phase field simulations also for boundary with comparatively large local curvatures. Significant deviations are seen for v_{ss} at a large λ and τ_{relax} at a small A .

Figure 10a shows the existence of a characteristic length

scale ℓ_c that separates regions with a constant v_{ss} and regions with an increasing v_{ss} . From the analytical analysis, this length scale is

$$\ell_c = \frac{M_0\sigma}{AF_s}, \quad (12)$$

as indicated by the vertical dashed lines for the two A values in Fig. 10a. It depends on the mobility perturbation amplitude A/M_0 , grain boundary energy, and stored energy. For a wavelength smaller than ℓ_c , v_{ss} remains mostly independent of λ , and the phase field results are in line with the analytical result:

$$v_{ss} = M_0F_s \sqrt{1 - \frac{A^2}{M_0^2}}, \quad (13)$$

which are shown by the dot-dashed lines for two different A in Fig. 10a. In this scenario, the mobility variations consistently introduce a drag effect (Fig. 10c). With larger A , *i.e.*, larger mobility variation, this drag effect is more pronounced than the one induced by variations in stored energy [32]. For example, for $A = 0.9M_0$ and $\lambda = 2 \mu\text{m}$, the mobility variation reduces velocity by a factor of 2.3 compared to the case without variation ($A = 0$).

Figure 10b shows the steady-state amplitude for different wavelengths, showing a good agreement between the phase field and the analytical results. From the analytical analysis, h_{ss} is proportional to λ^2 as

$$h_{ss} = \frac{g(A/M_0) F_s}{16 \sigma} \lambda^2, \quad (14)$$

where $g(\cdot)$ is given in Eq. A.5. Smaller λ results in a smoother boundary, *i.e.*, with smaller h_{ss} . Moreover, a smaller mobility perturbation amplitude, A , leads to a smoother steady-state boundary with a smaller h_{ss} (see Fig. 10e). Note $g(\cdot)$ is a monotonically increasing function, as demonstrated in Supplementary Fig. S9a.

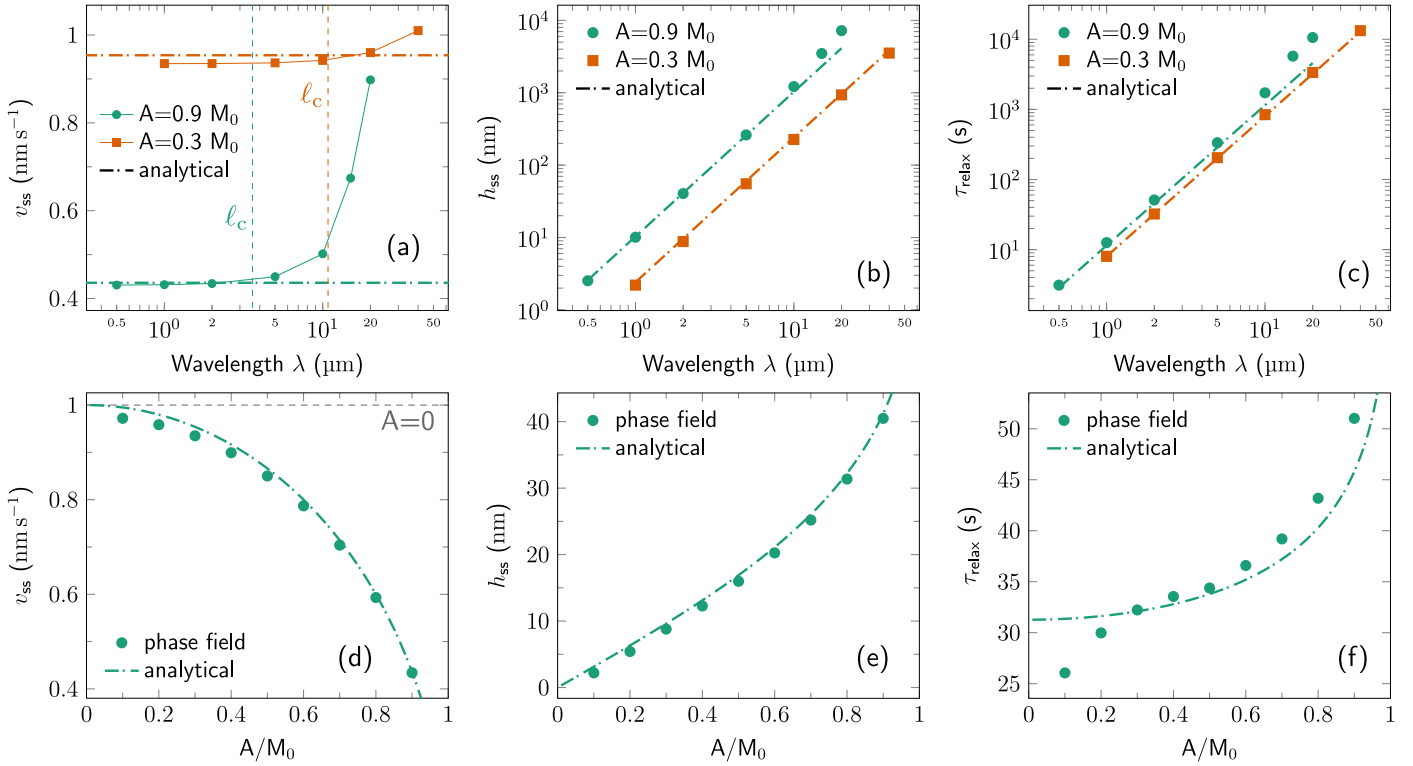


Fig. 10. Computational and theoretical analysis of the effect of spatial mobility variation on boundary migration. (a-c) The effect of mobility perturbation wavelength λ on the steady-state velocity v_{ss} (a), the steady-state amplitude h_{ss} (b), and the relaxation time τ_{relax} (c) for two mobility perturbation amplitudes A . (d-f) The effect of mobility perturbation amplitude A on the steady-state velocity v_{ss} (d), the steady-state amplitude h_{ss} (e), and the relaxation time τ_{relax} (f) for $\lambda = 2 \mu\text{m}$. Dot-dashed lines represent analytical solutions. The two vertical dashed lines in (a) mark the characteristic length scale ℓ_c .

The relaxation time τ_{relax} is shown as a function of λ and A/M_0 in Figs. 10c and 10f, respectively. This time characterizes how quickly a boundary can respond to the mobility variation and, as suggested by the analytical analysis, is also proportional to λ^2 :

$$\tau_{relax} = \frac{h_{ss}}{v_{ss}} \frac{\sqrt{M_0^2 - A^2}}{A}. \quad (15)$$

This equation captures the overall trend of τ_{relax} as a function of A/M_0 in Fig. 10f but fails for small A . τ_{relax} determined by phase field approaches zero as A goes zero. The discrepancy is a result of the approximation we used to derive Eq. 15.

When $\lambda > \ell_c$, more pronounced retrusions form. This is shown by a much larger h_{ss} and a greater curvature difference between the retrusion and protrusion (see Eq. A.6 and Supplementary Fig. S9b). Examples of the boundary morphology evolution can be seen in Supplementary Fig. S8. In this case, the assumption of small slope becomes less applicable, which explains the deviation between the phase-field and analytical results shown in Figs. 10a-c, especially for a large A . The development of large retrusions results in a boundary shape where most segments move at a high speed, weakening the drag effect. With a further increase in λ , it may eventually lead to an acceleration of boundary migration. However, the time required to reach the steady state, τ_{relax} , will be much longer. Before the boundary reaches a steady state, the average migration velocity is likely to be lower than that without mobility variation.

Despite the simplified mobility variation setup used in the

phase field simulation and analytical theory, the results provide valuable insights for interpreting the experimental results. For example, in Region 1 (later steps) and Region 2 in Fig. 7, the fitted mobility results suggest that A/M_0 is greater than 0.9 with a mobility perturbation wavelength of about 15-20 μm . The observed boundary amplitude h_{ss} aligns with the phase-field results in Fig. 10b. Additionally, the relaxation time is on the order of 10000 s (Fig. 10c), larger than the total annealing time for the present boundary. This suggests that the observed retrusions development in these two regions has not yet reached a steady state. The phase-field results indicate that with further annealing, the curvature driving force at those low-mobility segments will continue to increase, eventually allowing these segments to catch up with the faster-migration segments. In contrast, the relatively rapid boundary migration in the early steps in Region 1 corresponds to a mobility perturbation wavelength of about $\lambda = 5 \mu\text{m}$ and an amplitude of about $A/M_0 = 0.3$; see Fig. 7e. This behavior aligns with the theoretical prediction of a small drag effect (Fig. 10a), a perturbation amplitude h_{ss} of less than 1 μm (Fig. 10b), and a relaxation time of approximately 1000 s, which fits well within the experimental timescale of 4500 s.

Moreover, this analysis has suggested that the characteristic length scale ℓ_c may be used to evaluate the connectivity of local boundary segments. When mobility varies on a scale smaller than ℓ_c , the curvature driving force is sufficient for the low mobility boundary segments, allowing the boundary to move cohesively as a whole with a small perturbation amplitude. A smaller mobility perturbation A/M_0 results in a comparatively

larger ℓ_c (see Eq. 12), further flattening the boundary. This could explain the relatively flat boundary segments between the two boxed regions in Fig. 7. In this region, both the mobility perturbation amplitude and wavelength are small (λ is about $5 \mu\text{m}$ based on the local mobility pattern), resulting in an $\ell_c > \lambda$. On the other hand, when mobility varies over a distance much longer than ℓ_c , the curvature driving force is insufficient to maintain a smooth boundary, leading to the formation of large retrusions. A larger mobility perturbation A/M_0 decreases ℓ_c further, enhancing this effect.

Altogether, the analysis suggests that the mobility variation determined based on the average migration over long boundary segments might be underestimated compared to the mobility value averaged across all individual mobility values along the boundary segments. It should be noticed that the local stored energy variation also influences the recrystallization boundary, as revealed in Ref. [5, 32]. However, in a scenario where the stored-energy varies with a pattern in phase with the mobility variation, the stored energy is predicted to have no impact on v_{ss} (see Eq. B.2 in Appendix A). The combined effects of complex mobility and stored-energy variations require further detailed study in the future.

5. Conclusions and outlooks

This work proposes a fitting method for measuring the local variation of mobilities of recrystallized boundaries. Thousands of mobility values are determined simultaneously from a time-series recrystallization experiment. The results indicate that local mobility can vary by three orders of magnitude for the same recrystallization boundary, affecting the boundary morphology. By combining experimental, computational and theoretical analysis, we provide a comprehensive study of the effect of local mobility variation. The analytical expressions provide a simple yet powerful tool to understand the interplay between various factors on boundary migration. We find that small but fast spatial mobility variation results in a relatively smooth boundary, while large mobility variation over a long spatial distance leads to the development of large retrusion. A characteristic length scale is identified to distinguish these two boundary behaviors. This theoretical study helps to explain the experimentally observed recrystallization boundary migration dynamics, particularly boundary stagnation and connectivity. This work highlights that mobility variation can lead to an effective drag, adding to the understanding of drag effects due to impurities [33, 34], second-phase particles [35], and stored-energy variation [5, 32].

This novel fitting approach can be readily applied to other *in situ* recrystallization experiments, enabling the determination of mobilities for many recrystallization boundaries. By using more comprehensive experiments with improved spatial and temporal resolutions, the fitting quality can be further improved. While we have applied the proposed method to a 2D experiment, the fitting method can be extended to *in situ* 3D experiments that follow non-destructively the migration of the recrystallization front [29]. The measurement of the full 5D crystallography space (misorientation and inclination) can pro-

vide a complete picture of the effect of crystallography. In addition, the phase field simulation can be parallelized using MPI or GPU to utilize a grid size smaller than the experimental resolution.

Furthermore, recent studies have revealed significant residual stresses present within recrystallizing grains in several material systems using synchrotron micro-diffraction [36, 37, 38]. These stresses result from the redistribution of the medium-/long-range residual stresses developed in the deformed matrix [39, 40]. Once we know more about these local residual stresses, we can incorporate these elastic-stress driving forces to the model. Altogether, the present fitting method offers a unique opportunity to acquire a comprehensive set of materials mobility data, contributing to a thorough understanding of the recrystallization process.

Acknowledgments

YZ wishes to acknowledge the support of a research grant (VIL54495) from VILLUM FONDEN. This research was supported in part through the computational resources and staff contributions provided for the Quest high performance computing facility at Northwestern University which is jointly supported by the Office of the Provost, the Office for Research, and Northwestern University Information Technology.

Appendix A. Analytical analysis of the effect of mobility variation

To investigate the effect of spatial mobility variation, we assume a perturbation of the following form

$$M(x) = M_0 + A \cos(kx), \quad (\text{A.1})$$

where x is the coordinate, $k = 2\pi/\lambda$ is the wavenumber related to the wavelength λ , M_0 is the average mobility, and A quantifies the amplitude of the mobility perturbation. Since mobilities are all positive, we have $|A| < M_0$. Equation A.1 gives a banded mobility structure, as shown in Fig. 9a.

The velocity and shape of the boundary can be determined from Eq. 1. Assuming that the boundary reaches a steady state, let's denote $y(x)$ as the boundary profile, v_{ss} as the steady-state velocity, and h_{ss} as the steady-state perturbation amplitude. The velocity and curvature are $v = v_{ss}/\sqrt{1+(y')^2}$ and $\kappa = y''/(1+(y')^2)^{3/2}$, respectively. When $y'(x) \ll 1$, *i.e.*, the steady-state boundary is relatively flat, $v = v_{ss}$ and $\kappa = y''(x)$. Equation 1 then becomes a second-order ordinary differential equation. The profile $y(x)$ is defined in a moving frame with a velocity v_{ss} relative to the lab frame, so we have the boundary condition $y(0) = 0$. Due to the periodicity of $M(x)$ in Eq. A.1, the profile $y(x)$ is expected to have the same periodicity, leading to the periodic conditions $y'(0) = 0$ and $y'(\lambda/2) = 0$. The steady-state amplitude can be determined from $2h_{ss} = -y(\lambda/2)$. By solving the differential equation with the boundary and periodic conditions, we can obtain the steady-state velocity

$$v_{ss} = \sqrt{1 - \alpha^2 M_0 F_s} \quad (\text{A.2})$$

and the steady-state amplitude

$$h_{ss} = \frac{F_s}{16\sigma} g(\alpha) \lambda^2 \quad (\text{A.3})$$

where

$$\alpha = \frac{A}{M_0}, \quad (\text{A.4})$$

and

$$g(\alpha) = \frac{2}{\pi^2} \sqrt{\frac{1+\alpha}{1-\alpha}} \Phi\left(\frac{1+\alpha}{1-\alpha}, 2, \frac{1}{2}\right) + \frac{4}{\pi^2} \ln \frac{1-\alpha}{1+\alpha} \cdot \coth^{-1} \sqrt{\frac{1-\alpha}{1+\alpha}} - 1, \quad (\text{A.5})$$

where Φ represents Lerch's transcendent. Note that $g(0) = 0$ and $g(\alpha)$ is a monotonically increasing function of α , as shown in Supplementary Fig. S9a.

In Fig. 9a, we can observe that the low mobility boundaries (at $x = \lambda/2$) generally have a larger curvature than the high mobility boundaries (at $x = 0$ and $x = \lambda$). The ratio of curvatures $\eta = -y''(\lambda/2)/y''(0)$ is given by

$$\eta(\alpha) = \frac{\alpha + 1 - \sqrt{1 - \alpha^2}}{\alpha - 1 + \sqrt{1 - \alpha^2}}. \quad (\text{A.6})$$

Note that $\eta(0) = 1$, indicating a planar boundary, and η increases toward infinity as α approaches one. The shape of this η function is shown in Supplementary Fig. S9b.

The relaxation time of a boundary transitioning from a planar interface to the steady-state shape can be approximated, assuming a growth of a sinusoidal shape from $h = 0$ to $h = h_{ss}$. It can be derived as

$$\tau_{\text{relax}} = \frac{h_{ss}}{v_{ss}} \frac{\sqrt{1 - \alpha^2}}{\alpha}. \quad (\text{A.7})$$

A characteristic length scale ℓ_c can be related to a characteristic curvature $\kappa_c = 1/\ell_c$, which balances the stored energy and curvature driving forces between the fast and slow boundaries. Using Eq. 1 and $v_{\text{fast}} = v_{\text{slow}}$, it can be derived as

$$\ell_c = \frac{\sigma}{F_s \alpha}. \quad (\text{A.8})$$

Equation A.2 shows an effective drag due to mobility variation. When there is no mobility variation, $\alpha = 0$, the interface is planar ($h_{ss} = 0$ from Eq. A.2) and moves at a velocity of $v_{ss}^* = M_0 F_s$. According to Eq. A.2, any mobility variation $\alpha > 0$ leads to a drag $v_{ss} < v_{ss}^*$, and the boundary exhibits a larger curvature at retrusion ($x = \lambda/2$) compared to protrusion ($x = 0$ and $x = \lambda$), *i.e.*, $\eta > 1$. The wavelength of mobility variation λ does not affect v_{ss} (Eq. A.2). However, there is a second-order dependence of h_{ss} on λ (Eq. A.3), similar to the phase field result in Fig. 10b. From Eqs. A.7, A.2 and A.3, we see that τ_{relax} is proportional to λ^2 , consistent with the phase field result in Fig. 10c.

Appendix B. Analytical analysis with both mobility and stored-energy variations

For cases with both mobility and stored energy variations, if we assume the driving force has a perturbation that is in phase

with the mobility variation as defined in Eq. A.1

$$F_s(x) = F_0 - B \cos(kx), \quad (\text{B.1})$$

the differential equation provided in Eq. 1 can be solved similarly. The steady-state velocity is

$$v_{ss} = \sqrt{1 - \alpha^2} M_0 F_0. \quad (\text{B.2})$$

The steady-state amplitude is

$$h_{ss} = \frac{F_0}{16\sigma} \left(g(\alpha) - \frac{2}{\pi} \beta \right) \lambda^2, \quad (\text{B.3})$$

where

$$\beta = \frac{B}{F_0}. \quad (\text{B.4})$$

The ratio of curvatures is

$$\eta(\alpha) = \frac{\alpha + 1 - (1 + \beta) \sqrt{1 - \alpha^2}}{\alpha - 1 + (1 - \beta) \sqrt{1 - \alpha^2}}. \quad (\text{B.5})$$

Equation B.2 demonstrates that stored-energy variation β does not affect the steady-state velocity.

The characteristic length scale ℓ_c , in this case, is

$$\ell_c = \frac{\sigma}{F_0 |\alpha - \beta|}. \quad (\text{B.6})$$

Appendix C. Linear extension boundary condition

For a discretization u_{ij} , the boundary condition at the $j = 0$ boundary is

$$u_{i0} = 2u_{i1} - u_{i2}. \quad (\text{C.1})$$

Note that we use a cell-centered finite difference method. The boundary condition for the remaining boundaries can be expressed similarly.

References

- [1] R. Doherty, D. Hughes, F. Humphreys, J. J. Jonas, D. Juul Jensen, M. Kassner, W. King, T. McNelley, H. McQueen, A. Rollett, Current issues in recrystallization: a review, *Materials Science and Engineering: A* 238 (2) (1997) 219–274. doi:10.1016/S0921-5093(97)00424-3.
- [2] F. Haessner, *Recrystallization of Metallic Materials.*, Dr. Riederer Verlag, Stuttgart, 1978.
- [3] Y. Zhang, A. Godfrey, D. Juul Jensen, Local boundary migration during recrystallization in pure aluminium, *Scripta Materialia* 64 (2011) 331–334. doi:10.1016/j.scriptamat.2010.10.028.
- [4] Y. Zhang, A. Godfrey, D. Juul Jensen, In-situ investigation of local boundary migration during recrystallization, *Metallurgical and Materials Transactions A* 45 (2014) 2899–2905. doi:10.1007/s11661-014-2222-4.
- [5] N. Moelans, A. Godfrey, Y. Zhang, D. Juul Jensen, Phase-field simulation study of the migration of recrystallization boundaries, *Physical Review B* 88 (5) (2013) 054103. doi:10.1103/physrevb.88.054103.
- [6] V. Yadav, N. Moelans, Y. Zhang, D. Juul Jensen, Effects of dislocation boundary spacings and stored energy on boundary migration during recrystallization: A phase-field analysis, *Acta Materialia* 221 (2021). doi:10.1016/j.actamat.2021.117377.
- [7] G. Gottstein, D. Molodov, M. Winning, L. Shvindlerman, Grain boundary dynamics: A novel tool for microstructure control, *Interface Science* 9 (2001) 297–306. doi:10.1023/A:1015171130917.

- [8] D. Molodov, J. Swiderski, G. Gottstein, W. Lojkowski, L. Shvindlerman, Effect of pressure on grain boundary migration in aluminium bicrystals, *Acta Metallurgica et Materialia* 42 (10) (1994) 3397–3407. doi:10.1016/0956-7151(94)90472-3.
- [9] D. A. Molodov, T. Gorkaya, G. Gottstein, Migration of the $\Sigma 7$ tilt grain boundary in Al under an applied external stress, *Scripta Materialia* 65 (11) (2011) 990–993. doi:10.1016/j.scriptamat.2011.08.030.
- [10] M. Winning, G. Gottstein, L. Shvindlerman, On the mechanisms of grain boundary migration, *Acta Materialia* 50 (2002) 353–363. doi:10.1016/S1359-6454(01)00343-3.
- [11] H. Zhang, M. I. Mendeleev, D. J. Srolovitz, Mobility of $\sigma 5$ tilt grain boundaries: Inclination dependence, *Scripta Materialia* 52 (2005) 1193–1198. doi:10.1016/j.scriptamat.2005.03.012.
- [12] E. A. Holm, S. M. Foiles, How grain growth stops: a mechanism for grain-growth stagnation in pure materials., *Science* 328 (2010) 1138–41. doi:10.1126/science.1187833.
- [13] D. L. Olmsted, E. A. Holm, S. M. Foiles, Survey of computed grain boundary properties in face-centered cubic metals-II: Grain boundary mobility, *Acta Materialia* 57 (2009) 3704–3713. doi:10.1016/j.actamat.2009.04.015.
- [14] E. R. Homer, S. Patala, J. L. Priedeman, Grain boundary plane orientation fundamental zones and structure-property relationships, *Scientific Reports* 5 (2015) 15476. doi:10.1038/srep15476.
- [15] R. A. Vandermeer, D. Juul Jensen, E. Woldt, Grain boundary mobility during recrystallization of copper, *Metallurgical and Materials Transactions A* 28 (1997) 749–754. doi:10.1007/s11661-997-0061-2.
- [16] Y. Huang, F. Humphreys, Measurements of grain boundary mobility during recrystallization of a single-phase aluminium alloy, *Acta Materialia* 47 (7) (1999) 2259–2268. doi:10.1016/S1359-6454(99)00062-2.
- [17] M. L. Taheri, A. D. Rollett, H. Weiland, In-situ quantification of solute effects on grain boundary mobility and character in aluminum alloys during recrystallization, *Materials Science Forum* 467-470 (2004) 997–1002. doi:10.4028/www.scientific.net/MSF.467-470.997.
- [18] A. Lens, C. Maurice, J. Driver, Grain boundary mobilities during recrystallization of Al-Mn alloys as measured by in situ annealing experiments, *Materials Science and Engineering: A* 403 (2005) 144–153. doi:10.1016/j.msea.2005.05.010.
- [19] Y. Zhang, Quantification of local mobilities, *Scripta Materialia* 146 (2018) 286–289. doi:10.1016/j.scriptamat.2017.12.012.
- [20] I. Basu, M. Chen, M. Loeck, T. Al-Samman, D. A. Molodov, Determination of grain boundary mobility during recrystallization by statistical evaluation of electron backscatter diffraction measurements, *Materials Characterization* 117 (2016) 99–112. doi:10.1016/j.matchar.2016.04.024.
- [21] Y. Huang, F. J. Humphreys, The effect of solutes on grain boundary mobility during recrystallization and grain growth in some single-phase aluminium alloys, *Materials Chemistry and Physics* 132 (2012) 166–174. doi:10.1016/j.matchemphys.2011.11.018.
- [22] J. Zhang, S. O. Poulsen, J. W. Gibbs, P. W. Voorhees, H. F. Poulsen, Determining material parameters using phase-field simulations and experiments, *Acta Materialia* 129 (2017) 229–238. doi:10.1016/j.actamat.2017.02.056.
- [23] J. Zhang, W. Ludwig, Y. Zhang, H. H. B. Sørensen, D. J. Rowenhorst, A. Yamanaka, P. W. Voorhees, H. F. Poulsen, Grain boundary mobilities in polycrystals, *Acta Materialia* 191 (2020) 211–220. doi:10.1016/j.actamat.2020.03.044.
- [24] J. Zhang, A. F. Chadwick, D. L. Chopp, P. W. Voorhees, Phase field modeling with large driving forces, *npj Computational Materials* 9 (166) (2023). doi:10.1038/s41524-023-01118-0.
- [25] M. P. Bendsøe, O. Sigmund, *Topology optimization: theory, methods, and applications*, Springer Science & Business Media, 2003.
- [26] J. Zhang, Determination of material parameters by comparison of 3D simulations and 3D experiments, Ph.D. thesis, Technical University of Denmark (2018).
- [27] F. Humphreys, A unified theory of recovery, recrystallization and grain growth, based on the stability and growth of cellular microstructures - I. the basic model, *Acta Materialia* 45 (10) (1997) 4231–4240. doi:10.1016/S1359-6454(97)00070-0.
- [28] Y. B. Zhang, A. Elbrønd, F. X. Lin, A method to correct coordinate distortion in EBSD maps, *Materials Characterization* 96 (2014) 158–165. doi:10.1016/j.matchar.2014.08.003.
- [29] Y. Zhang, J. D. Budai, J. Z. Tischler, W. Liu, R. Xu, E. Homer, A. Godfrey, D. Juul Jensen, Boundary migration in a 3D deformed microstructure inside an opaque sample, *Scientific Reports* 7 (1) (2017) 4423.
- [30] F. J. Humphreys, P. S. Bate, P. J. Hurley, Orientation averaging of electron backscattered diffraction data, *Journal of Microscopy* 201 (2001) 50–58. doi:10.1046/j.1365-2818.2001.00777.x.
- [31] M. Kuwahara, K. Hachimura, S. Eiho, M. Kinoshita, Digital processing of biomedical images, chapter processing of ri-angiocardigraphic images, Plenum Press 160 (1976) 187–203.
- [32] N. Moelans, Y. B. Zhang, A. Godfrey, D. Juul Jensen, A phase-field simulation study of irregular grain boundary migration during recrystallization, *IOP Conference Series: Materials Science and Engineering* 89 (2015) 012037. doi:10.1088/1757-899x/89/1/012037.
- [33] J. W. Cahn, The impurity-drag effect in grain boundary motion, *Acta Metallurgica* 10 (9) (1962) 789–798. doi:10.1016/0001-6160(62)90092-5.
- [34] G. Gottstein, L. S. Shvindlerman, *Grain boundary migration in metals: thermodynamics, kinetics, applications*, CRC press, 2009.
- [35] C. Smith, *Grains, phases and interfaces: Interpretation of microstructures*, Transaction metallurgy Society of AIME 175 (1948) 15–51. doi:10.1007/s11661-010-0215-5.
- [36] Y. Zhang, T. Yu, R. Xu, J. Thorborg, W. Liu, J. Tischler, A. Godfrey, D. Juul Jensen, Local residual stresses and microstructure within recrystallizing grains in iron, *Materials Characterization* 191 (2022) 112113. doi:10.2139/ssrn.4051529.
- [37] A. Lindkvist, W. Liu, D. Juul Jensen, Y. Zhang, 3D mapping of residual stresses in growing grains of partially recrystallized gum metal, *Materials Research Letters* 11 (2023) 942–948. doi:10.2139/ssrn.4153555.
- [38] Y. Zhang, W. Ludwig, Selective growth of recrystallizing grains into well-characterized deformed aluminum at hardness indentation, *Acta Materialia* 270 (2024) 119862. doi:http://dx.doi.org/10.2139/ssrn.4603490.
- [39] I. F. Lee, T. Q. Phan, L. E. Levine, J. Z. Tischler, P. T. Geantil, Y. Huang, T. G. Langdon, M. E. Kassner, Using x-ray microbeam diffraction to study the long-range internal stresses in aluminum processed by ECAP, *Acta Materialia* 61 (2013) 7741–7748. doi:10.1016/j.actamat.2013.09.013.
- [40] M. E. Kassner, P. Geantil, L. E. Levine, Long range internal stresses in single-phase crystalline materials, *International Journal of Plasticity* 45 (2013) 44–60. doi:10.1016/j.ijplas.2012.10.003.